Direct CALPHAD coupling phase-field model: Closed-form expression for interface composition satisfying equal diffusion potential condition

Takumi Morino [*]

Yokohama National University, 79-5 Tokiwadai, Hodogayaku, Yokohama 240-8501, Japan

Machiko Ode

National Institute for Materials Science, 1-2-1 Sengen, Tsukuba, Ibaraki 305-0047, Japan

Shoichi Hirosawa

Department of Mechanical Engineering and Materials Science, Yokohama National University, 79-5 Tokiwadai, Hodogayaku, Yokohama 240-8501, Japan

We formulated two phase-field models to compute interfacial compositions, characterized by their high computational accuracy and efficiency. The inaugural model utilizes convergence calculations to fulfill the equal diffusion potential condition, while the subsequent model obviates the need for such calculations. Despite this, its computational outcomes strongly agree with those of the preceding model. Notably, in these models, the alteration in composition attributable to interfacial curvatures aligns with the Gibbs-Thomson effect within the equilibrium system. In this study, the solidification processes of Ni-Al-Cr and Ag-Cu-Sn alloys serve as case studies to underscore the computational precision and swiftness of the proposed models.

I. INTRODUCTION

The phase-field model, renowned for its efficacy in addressing free-boundary problems within materials science and engineering, has garnered significant interest following Kobayashi's pioneering simulation of dendritic growth in pure materials [1]. This model has since evolved to encompass binary [2–4] systems and multicomponent [5] and multiphase [6–8] systems. Its integration with the calculation of phase diagrams (CALPHAD) approach has enabled the simulation of microstructure evolution in practical alloys [9–13]. The computational cost of CALPHAD integration greatly depends on how the interfacial composition is handled. In the Wheeler-Boettinger-McFadden (WBM) model [2], the interfacial region is assumed to be a mixture of multiple phases with the same composition. Coupling the CALPHAD database with the WBM model is straightforward because there is no need to utilize additional conditions to determine the interfacial composition. However, the chemical energy in this model is a double-well-type function with respect to composition, resulting in excess energy in the interfacial region.

To remove this spurious energy, the Kim-Kim-Suzuki (KKS) model [4] considers solute partitioning at the interfacial region such that the coexisting solid and liquid phases have different compositions. This partitioning is performed under the assumption that local equilibrium is maintained in the interfacial region (i.e., an equal diffusion potential

condition). Nonetheless, determining compositions satisfying the equal diffusion potential condition is time consuming because of the complexities of regular solution functions described by the Redlich-Kister polynomial, which is extensively used in the CALPHAD approach to specify the excess Gibbs energy. To mitigate computational demands, various strategies have been introduced. Kobayashi *et al.* proposed a method to precompile a database of potential equal diffusion compositions, thereby circumventing the need to resolve nonlinear equations midsimulation [11]. Additionally, extrapolation techniques, such as the "diagonal" and "multibinary" approaches [14–16], enhance computational efficiency by limiting thermodynamic calculations to specific intervals and extrapolating quasiequilibrium data until subsequent evaluations. While these methods offer a versatile framework for software integration and aim to balance computational speed with accuracy, they inherently face a tradeoff between reducing computation times and increasing precision. Moreover, these approaches fail to accurately account for the curvature effect, a critical factor in the evolution of microscale microstructures. Beyond these approaches, strategies, including a parabolic approximation of free energy functions [17,18] and the incorporation of machine learning [19,20], have been proposed to expedite computations within the KKS model framework. Nonetheless, the effectiveness of the former is limited in multicomponent systems, while the latter necessitates extensive preprocessing of equilibrium data. Compiling equilibrium data across diverse temperatures and compositions proves particularly challenging in systems with three or more components owing to multiple equilibrium states.

*morino-takumi-rb@ynu.jp

The finite interface dissipation (FID) model [21,22] assumes that the interfacial region is a mixture of multiple phases with different compositions and diffusion potentials. This model was introduced to elucidate rapid solidification phenomena where the equal diffusion potential condition is not applicable, offering a framework to accommodate discontinuities in chemical potential across interfaces. In the FID model, the solute partitioning in the interfaces is determined by the variational derivative of the total free energy with respect to the interface concentration. The calculation of the partitioning equation is straightforward even with CALPHAD functions, thereby ensuring that the computational cost associated with CALPHAD integration with the FID model is as low as that of the WBM model. The interfacial permeability P, which defines the degree of nonequilibrium in the FID model, indicates that a smaller value corresponds to a higher degree of nonequilibrium, while a sufficiently large value can also replicate local equilibrium conditions. Therefore, the FID model, even when coupled with CALPHAD, may be used to perform phase-field simulations under local equilibrium conditions at a low computational cost [23,24]. Although theoretical constructs allow for assigning exceedingly large values to physical quantities, practical numerical computations encounter difficulties when handling such values. To maintain numerical stability, interfacial permeability must be maintained within a moderate range, precluding the assurance of equal diffusion potentials. Additionally, the FID model encounters issues in integrating the anti-trapping current [25,26] necessary for precise quantitative analysis.

The aim of this study is to overcome the long-standing lack of a method for effectively solving the equal diffusion condition as this condition is a prerequisite for most microstructure evolution phenomena. An optimal model for implementing equal diffusion potential conditions that is versatile enough to apply across various thermodynamic systems while ensuring computational accuracy and efficiency is desired. Specifically, such a model must fulfill four critical criteria: (i) Eliminate the need for preliminary calculations, such as those reliant on machine learning; (ii) unequivocally ensure equal diffusion potential conditions; (iii) facilitate the direct application of CALPHAD functions, and (iv) obviate the necessity for additional parameters, including interfacial permeability as seen in the FID model and recalibration intervals characteristic of the extrapolation method. We derived two models aimed at achieving equal diffusion potential conditions by adapting the governing equations of the FID model. The first model, referred to as the iterative model, utilizes convergence calculations to meet the equal diffusion potential condition. In contrast, the second model, known as the noniterative model, is designed to bypass the need for such calculations. These models can be referred to as the "direct CALPHAD coupling phase-field models," which allow for a direct coupling of the CALPHAD database with the phase-field method. To validate the efficacy of the direct CALPHAD coupling phase-field model, we examined the Gibbs-Thomson effect and steady-state conditions. Additionally, the microstructural evolution of Ni-Al-Cr and Ag-Cu-Sn alloys was simulated, further demonstrating the capabilities of the developed models.

The foundational equation of the FID model, as formulated by Steinbach *et al.*, posits that compositional changes at the interface [21,22] are minimal, a constraint driven by the model's aim to replicate the solute trapping effect observed during rapid solidification processes. Contrasting this initial premise, Koyama expanded the model's applicability by relaxing this assumption, enabling its application to form grain boundary phases [27]. Building upon this modification, we have embraced a more flexible formulation and derived the governing equation pertinent to N phases.

II. MODEL DESCRIPTION

A. FID model

The total free energy functional in a multicomponent and multiphase alloy is given by

$$
F = \int_V \left[\sum_{\alpha=1}^{N} \sum_{\beta=\alpha+1}^{N} \left(-\frac{a_{\alpha\beta}^2}{2} \nabla\phi_\alpha \cdot \nabla\phi_\beta \right) \right.
$$
$$
+ \sum_{\alpha=1}^{N} \sum_{\beta=\alpha+1}^{N} (W_{\alpha\beta}\phi_\alpha\phi_\beta)
$$
$$
\left. + \sum_{\alpha=1}^{N} \phi_\alpha f_\alpha + \sum_{i=1}^{n-1} \lambda^i \left(c^i - \sum_{\alpha=1}^{N} \phi_\alpha c_\alpha^i \right) \right] dV, \quad (1)
$$

where c^i is the composition field (solvent $i = n$ and solute $i = 1, \ldots, n-1$), ϕ_α is the phase-field variable that gives the local fraction of phase α ($\alpha = 1, \ldots, N$ phases), c_α^i is the phase composition of component i of phase α, f_α is the chemical free energy density of phase α, and λ^i is a Lagrange multiplier that is used to consider the solute conservation constraint, as follows:

$$
c^i = \sum_{\alpha=1}^{N} \phi_\alpha c_\alpha^i, \quad (2)
$$

where $a_{\alpha\beta} = \sqrt{2\delta_{\alpha\beta}\sigma_{\alpha\beta}}$ and $W_{\alpha\beta} = 4\frac{\sigma_{\alpha\beta}}{\delta_{\alpha\beta}}$ are the gradient coefficient and height of double-obstacle potential between phases α and β, respectively. $\delta_{\alpha\beta}$ and $\sigma_{\alpha\beta}$ are the interface thickness and interface energy between phases α and β, respectively. The governing equation of the phase composition was obtained using the variational derivative:

$$
\frac{\partial c_\alpha^i}{\partial t} = -\sum_{j=1}^{n-1} P^{ij}(\phi_\alpha) \frac{\delta F}{\delta c_\alpha^j} = -\sum_{j=1}^{n-1} P^{ij}(\phi_\alpha) \phi_\alpha \left(\frac{\partial f_\alpha}{\partial c_\alpha^j} - \lambda^j \right).
$$
$$
(3)
$$

where $P^{ij}(\phi_\alpha)$ is the interface permeability [21]. Assuming that $P^{ij}(\phi_\alpha)\phi_\alpha$ is a constant P^{ij} and that the permeability matrix is a diagonal $P^i = \delta_{ij} P^{ij}$, where δ_{ij} is the Kronecker delta ($\delta_{ij} = 1$ if $i = j$, otherwise $\delta_{ij} = 0$), Eq. (3) can be expressed as follows:

$$
\frac{\partial c_\alpha^i}{\partial t} = -P^i \left(\frac{\partial f_\alpha}{\partial c_\alpha^i} - \lambda^i \right). \quad (4)
$$

Therefore, an expression for λ^i is obtained by differentiating Eq. (2) with time and substituting Eq. (4) into it:

$$
\frac{\partial c^i}{\partial t} = \sum_{\alpha=1}^{N} \frac{\partial \phi_\alpha}{\partial t} c_\alpha^i + \sum_{\alpha=1}^{N} \phi_\alpha \frac{\partial c_\alpha^i}{\partial t}
$$

$$
= \sum_{\alpha=1}^{N} \frac{\partial \phi_\alpha}{\partial t} c_\alpha^i - P^i \sum_{\alpha=1}^{N} \phi_\alpha \frac{\partial f_\alpha}{\partial c_\alpha^i} + P^i \lambda^i \tag{5a}
$$

$$
\therefore \lambda^i = \sum_{\alpha=1}^{N} \phi_\alpha \frac{\partial f_\alpha}{\partial c_\alpha^j} - \frac{1}{P^i} \left(\sum_{\alpha=1}^{N} \frac{\partial \phi_\alpha}{\partial t} c_\alpha^i - \frac{\partial c^i}{\partial t} \right). \tag{5b}
$$

By substituting Eq. (5b) into Eq. (4), the governing equation for the phase composition was obtained as follows:

$$
\frac{\partial c_\alpha^i}{\partial t} = -P^i \left\{ \frac{\partial f_\alpha}{\partial c_\alpha^i} - \left[\sum_{\beta=1}^{N} \phi_\beta \frac{\partial f_\beta}{\partial c_\beta^i} \right. \right.
$$

$$
\left. \left. - \frac{1}{P^i} \left(\sum_{\beta=1}^{N} \frac{\partial \phi_\beta}{\partial t} c_\beta^i - \frac{\partial c^i}{\partial t} \right) \right] \right\} \tag{6a}
$$

$$
= -P^i \sum_{\beta=1}^{N} \phi_\beta \left(\frac{\partial f_\alpha}{\partial c_\alpha^i} - \frac{\partial f_\beta}{\partial c_\beta^i} \right) - \sum_{\beta=1}^{N} \frac{\partial \phi_\beta}{\partial t} c_\beta^i + \frac{\partial c^i}{\partial t}. \tag{6b}
$$

Using the finite difference method, the change in phase composition after a time interval Δt can be expressed as follows:

$$
\Delta c_\alpha^i = \sum_{\beta=1}^{N} {}_{\text{exchange}} \Delta c_{\alpha\beta}^i + {}_{\text{conserve}} \Delta c_\alpha^i. \tag{7}
$$

In this study, the first term of Eq. (7) is the "exchange term," which describes the flux of component exchange between phases α and β:

$$
{}_{\text{exchange}} \Delta c_{\alpha\beta}^i = -P^i \phi_\beta \left(\frac{\partial f_\alpha}{\partial c_\alpha^i} - \frac{\partial f_\beta}{\partial c_\beta^i} \right) \Delta t. \tag{8}
$$

Similarly, we refer to the second term in Eq. (7) as the "conservation term," which describes the conservation constraint of compositions during the evolution of the phase field and composition field:

$$
{}_{\text{conserve}} \Delta c_\alpha^i = \left(- \sum_{\beta=1}^{N} \frac{\partial \phi_\beta}{\partial t} c_\beta^i + \frac{\partial c^i}{\partial t} \right) \Delta t. \tag{9}
$$

The governing equation for the multiphase-field model is expressed as follows:

$$
\frac{\partial \phi_\alpha}{\partial t} = -\frac{2}{N} \sum_{\beta=1}^{N} M_{\alpha\beta} \left(\frac{\delta F}{\delta \phi_\alpha} - \frac{\delta F}{\delta \phi_\beta} \right) \tag{10a}
$$

$$
= -\frac{2}{N} \sum_{\beta=1}^{N} M_{\alpha\beta} \left\{ \sum_{\gamma=1}^{N} \left[(W_{\alpha\gamma} - W_{\beta\gamma}) \phi_\gamma + \frac{1}{2} (a_{\alpha\gamma}^2 - a_{\beta\gamma}^2) \nabla^2 \phi_\gamma \right] \right.
$$

$$
\left. + f_\alpha - f_\beta - \sum_{i=1}^{n-1} \left[\sum_{\alpha=1}^{N} \phi_\alpha \frac{\partial f_\alpha}{\partial c_\alpha^i} - \frac{1}{P^i} \left(\sum_{\alpha=1}^{N} \frac{\partial \phi_\alpha}{\partial t} c_\alpha^i - \frac{\partial c^i}{\partial t} \right) \right] (c_\alpha^i - c_\beta^i) \right\}, \tag{10b}
$$

where $M_{\alpha\beta}$ is the mobility of the phase-field variable between phases α and β.

B. Iterative model

In the FID model, it is necessary to set a sufficiently large interface permeability value to achieve equal diffusion potential conditions, however, this makes the numerical calculations unstable and does not guarantee equal diffusion potential conditions. Therefore, this section proposes a method that adds an iterative calculation for the exchange term ${}_{\text{exchange}}^{\text{new}} \Delta c_{\alpha\beta}^i$ to satisfy the equal diffusion potential condition of interfacial compositions without large interface permeability.

We describe the composition (differing from the phase composition) transfer from phase β to phase α as $\phi_\alpha \phi_\beta x^i$. x^i is a variable related to solute i. The phase compositions of component i in phases α and β after Δt owing to the exchange term can be described as

$$
c_\alpha^i \big|_{t+\Delta t} = c_\alpha^i \big|_t + {}_{\text{exchange}}^{\text{new}} \Delta c_{\alpha\beta}^i = c_\alpha^i \big|_t + \frac{\phi_\alpha \phi_\beta x^i}{\phi_\alpha}, \tag{11}
$$

$$
c_\beta^i \big|_{t+\Delta t} = c_\beta^i \big|_t + {}_{\text{exchange}}^{\text{new}} \Delta c_{\beta\alpha}^i = c_\beta^i \big|_t - \frac{\phi_\alpha \phi_\beta x^i}{\phi_\beta}. \tag{12}
$$

It is noteworthy that the composition change divided by the phase-field variable corresponds to the phase composition change. We define a diffusion potential difference function H^i, which corresponds to the difference in diffusion potential for component i between phases α and β, as follows:

$$
H^i(x^1, \ldots, x^{n-1}) = \frac{\partial f_\alpha}{\partial c_\alpha^i} \left(c_\alpha^1 \big|_{t+\Delta t}, \ldots, c_\alpha^{n-1} \big|_{t+\Delta t} \right) - \frac{\partial f_\beta}{\partial c_\beta^i} \left(c_\beta^1 \big|_{t+\Delta t}, \ldots, c_\beta^{n-1} \big|_{t+\Delta t} \right). \tag{13}
$$

The Maclaurin expansion of Eq. (13) is given by a series of

$$H^i(x^1, \ldots, x^{n-1}) = \sum_{k=0}^{\infty} \frac{1}{k!} \left(x^1 \frac{\partial}{\partial x^1} + \cdots + x^{n-1} \frac{\partial}{\partial x^{n-1}} \right)^k H^i(0, \ldots, 0) \tag{14a}$$

$$= \sum_{k=0}^{\infty} \frac{1}{k!} \left(x^1 \frac{\partial}{\partial x^1} + \cdots + x^{n-1} \frac{\partial}{\partial x^{n-1}} \right)^k \left[\frac{\partial f_\alpha}{\partial c_\alpha^i} \left(c_\alpha^1 \big|_t, \ldots, c_\alpha^{n-1} \big|_t \right) - \frac{\partial f_\beta}{\partial c_\beta^i} \left(c_\beta^1 \big|_t, \ldots, c_\beta^{n-1} \big|_t \right) \right]. \tag{14b}$$

When we ignore the second and higher orders of k and apply the chain rule, Eq. (14b) can be written as follows (see Appendix A for more detail):

$$H^i(x^1, \ldots, x^{n-1}) = \frac{\partial f_\alpha}{\partial c_\alpha^i} \left(c_\alpha^1 \big|_t, \ldots, c_\alpha^{n-1} \big|_t \right) - \frac{\partial f_\beta}{\partial c_\beta^i} \left(c_\beta^1 \big|_t, \ldots, c_\beta^{n-1} \big|_t \right) + \phi_\beta \left(x^1 \frac{\partial}{\partial c_\alpha^1} + \cdots + x^{n-1} \frac{\partial}{\partial c_\alpha^{n-1}} \right) \frac{\partial f_\alpha}{\partial c_\alpha^i} \left(c_\alpha^1 \big|_t, \ldots, c_\alpha^{n-1} \big|_t \right)$$

$$+ \phi_\alpha \left(x^1 \frac{\partial}{\partial c_\beta^1} + \cdots + x^{n-1} \frac{\partial}{\partial c_\beta^{n-1}} \right) \frac{\partial f_\beta}{\partial c_\beta^i} \left(c_\beta^1 \big|_t, \ldots, c_\beta^{n-1} \big|_t \right). \tag{15}$$

Considering the equal diffusion potential condition ($H^i = 0$) and neglecting the cross terms, Eq. (15) can be solved analytically with respect to x^i to obtain the following simple form:

$$\therefore x^i = -\frac{\frac{\partial f_\alpha}{\partial c_\alpha^i} - \frac{\partial f_\beta}{\partial c_\beta^i}}{\phi_\beta \frac{\partial^2 f_\alpha}{(\partial c_\alpha^i)^2} + \phi_\alpha \frac{\partial^2 f_\beta}{(\partial c_\beta^i)^2}}, \tag{16}$$

resulting in a significantly reduced computation time. This approximation applies to most alloys. An analytical solution with respect to x^i can also be obtained without neglecting the cross terms, as described in Appendix B. Equations (11) and (16) yield the following exchange term:

$$^{\text{new}}_{\text{exchange}} \Delta c_{\alpha\beta}^i = -\frac{\frac{\partial f_\alpha}{\partial c_\alpha^i} - \frac{\partial f_\beta}{\partial c_\beta^i}}{\phi_\beta \frac{\partial^2 f_\alpha}{(\partial c_\alpha^i)^2} + \phi_\alpha \frac{\partial^2 f_\beta}{(\partial c_\beta^i)^2}} \phi_\beta. \tag{17}$$

The diffusion potentials of the α and β phases coincide. In the iterative model, Eq. (17) is solved repeatedly to guarantee equal diffusion potential conditions. By applying an infinite interface permeability and equal diffusion potential conditions to Eq. (10b), the phase-field governing equation can be modified as

$$\frac{\partial \phi_\alpha}{\partial t} = -\frac{2}{N} \sum_{\beta=1}^{N} M_{\alpha\beta} \left\{ \sum_{\gamma=1}^{N} \left[(W_{\alpha\gamma} - W_{\beta\gamma}) \phi_\gamma \right. \right.$$

$$+ \frac{1}{2} \left(a_{\alpha\gamma}^2 - a_{\beta\gamma}^2 \right) \nabla^2 \phi_\gamma \bigg]$$

$$\left. + f_\alpha - f_\beta - \sum_{i=1}^{n-1} \frac{\partial f_\alpha}{\partial c_\alpha^i} \left(c_\alpha^i - c_\beta^i \right) \right\}. \tag{18}$$

Calculations under an equal diffusion potential condition are feasible without setting the interface permeability in the iterative model. It is noteworthy that Eq. (17) is obtained by assuming a constant value of the phase-field variable, therefore the exchange term must be computed separately from the phase-field equations. Physically, this implies that the exchange of components occurs more rapidly than the

development of the phase-field variable. The iterative model is equivalent to the standard multiphase-field with quasiequilibrium model. This is because the iterative model satisfies the equal diffusion potential condition by iterative exchange and employs the standard multiphase-field evolution equation for the phase-field variable as well as the conservation term of FID, which can be reduced to obtain the standard multiphase-field evolution equation of composition.

C. Noniterative model

The exchange term was modified in the previous section to achieve a fully equal diffusion potential in the interface-partitioning calculation. This section focuses on the conservation term $_{\text{conserve}} \Delta c_\alpha^i$ to develop a noniterative model. The conservation term often induces a deviation of interface phase compositions from the equal diffusion potential condition. We modify the conservation term by introducing a partition coefficient into the conservation constraint. This approach can correct deviations from the equal diffusion potential condition without convergence calculations for the exchange term.

In the noniterative model, the relationship between the compositions of phases α and β is obtained by following the process described in [14],

$$^{\text{new}}_{\text{conserve}} \Delta c_\beta^i = ^{\text{new}}_{\text{conserve}} \Delta c_\alpha^i k_{\beta\alpha}^i, \tag{19}$$

where $k_{\beta\alpha}^i$ is the partition coefficient of the component i between phases β and α. The conservation equation represented by Eq. (2) after a time interval Δt is expressed as

$$\sum_{\beta=1}^{N} c_\beta^i \phi_\beta + \frac{\partial c^i}{\partial t} \Delta t = \sum_{\beta=1}^{N} \left(c_\beta^i + ^{\text{new}}_{\text{conserve}} \Delta c_\beta^i \right) \left(\phi_\beta + \frac{\partial \phi_\beta}{\partial t} \Delta t \right). \tag{20}$$

Substituting Eq. (19) into Eq. (20) yields the following equation:

$$^{\text{new}}_{\text{conserve}} \Delta c_\alpha^i = \frac{\sum_{\beta=1}^{N} c_\beta^i \phi_\beta + \frac{\partial c^i}{\partial t} \Delta t - \sum_{\beta=1}^{N} c_\beta^i \left(\phi_\beta + \frac{\partial \phi_\beta}{\partial t} \Delta t \right)}{\sum_{\beta=1}^{N} k_{\beta\alpha}^i \left(\phi_\beta + \frac{\partial \phi_\beta}{\partial t} \Delta t \right)}. \tag{21}$$

The partition coefficient can be derived in the same manner as in the previous section. The phase compositions of component i for phases α and β after Δt owing to the conservation term can be described as

$$c_\alpha^i \big|_{t+\Delta t} = c_\alpha^i \big|_t + \underset{\text{conserve}}{\text{new}} \Delta c_\alpha^i, \tag{22}$$

$$c_\beta^i \big|_{t+\Delta t} = c_\beta^i \big|_t + \underset{\text{conserve}}{\text{new}} \Delta c_\beta^i = c_\beta^i \big|_t + \underset{\text{conserve}}{\text{new}} \Delta c_\alpha^i k_{\beta\alpha}^i. \tag{23}$$

We define a diffusion potential difference function H^i, which corresponds to a difference in diffusion potential for component i between phases α and β, as follows:

$$\begin{aligned}
H^i &\left(\underset{\text{conserve}}{\text{new}} \Delta c_\alpha^1, \ldots, \underset{\text{conserve}}{\text{new}} \Delta c_\alpha^{n-1} \right) \\
&= \frac{\partial f_\alpha}{\partial c_\alpha^i} \left(c_\alpha^1 \big|_{t+\Delta t}, \ldots, c_\alpha^{n-1} \big|_{t+\Delta t} \right) \\
&\quad - \frac{\partial f_\beta}{\partial c_\beta^i} \left(c_\beta^1 \big|_{t+\Delta t}, \ldots, c_\beta^{n-1} \big|_{t+\Delta t} \right).
\end{aligned} \tag{24}$$

When we ignore the second and higher orders of k and the cross terms in the Maclaurin expansion of Eq. (24), the diffusion potential difference function takes the following form:

$$\begin{aligned}
H^i &\left(\underset{\text{conserve}}{\text{new}} \Delta c_\alpha^1, \ldots, \underset{\text{conserve}}{\text{new}} \Delta c_\alpha^{n-1} \right) \\
&= \frac{\partial f_\alpha}{\partial c_\alpha^i} \left(c_\alpha^1 \big|_t, \ldots, c_\alpha^{n-1} \big|_t \right) \\
&\quad - \frac{\partial f_\beta}{\partial c_\beta^i} \left(c_\beta^1 \big|_t, \ldots, c_\beta^{n-1} \big|_t \right) \\
&\quad + \underset{\text{conserve}}{\text{new}} \Delta c_\alpha^i \frac{\partial^2 f_\alpha}{\left(\partial c_\alpha^i \right)^2} \left(c_\alpha^1 \big|_t, \ldots, c_\alpha^{n-1} \big|_t \right) \\
&\quad - \underset{\text{conserve}}{\text{new}} \Delta c_\alpha^i k_{\beta\alpha}^i \frac{\partial^2 f_\beta}{\left(\partial c_\beta^i \right)^2} \left(c_\beta^1 \big|_t, \ldots, c_\beta^{n-1} \big|_t \right).
\end{aligned} \tag{25}$$

By considering the equal diffusion potential condition at $t + \Delta t$ ($H^i = 0$), the partition coefficient can be described as

$$k_{\beta\alpha}^i = \frac{\dfrac{\partial f_\alpha}{\partial c_\alpha^i} - \dfrac{\partial f_\beta}{\partial c_\beta^i} + \underset{\text{conserve}}{\text{new}} \Delta c_\alpha^i \dfrac{\partial^2 f_\alpha}{\left(\partial c_\alpha^i \right)^2}}{\underset{\text{conserve}}{\text{new}} \Delta c_\alpha^i \dfrac{\partial^2 f_\beta}{\left(\partial c_\beta^i \right)^2}}. \tag{26}$$

The equal diffusion potential condition at t $\left(\frac{\partial f_\alpha}{\partial c_\alpha^i} - \frac{\partial f_\beta}{\partial c_\beta^i} \right)$ and Eq. (26) yield the simplified form of the partition coefficient:

$$k_{\beta\alpha}^i = \frac{\partial^2 f_\alpha}{\left(\partial c_\alpha^i \right)^2} \bigg/ \frac{\partial^2 f_\beta}{\left(\partial c_\beta^i \right)^2}. \tag{27}$$

By using this partition coefficient, Eq. (21) can be expressed as follows:

$$\underset{\text{conserve}}{\text{new}} \Delta c_\alpha^i = \frac{\sum_{\beta=1}^N c_\beta^i \phi_\beta + \frac{\partial c^i}{\partial t} \Delta t - \sum_{\beta=1}^N c_\beta^i \left(\phi_\beta + \frac{\partial \phi_\beta}{\partial t} \Delta t \right)}{\sum_{\beta=1}^N \frac{\partial^2 f_\alpha}{\left(\partial c_\alpha^i \right)^2} \bigg/ \frac{\partial^2 f_\beta}{\left(\partial c_\beta^i \right)^2} \left(\phi_\beta + \frac{\partial \phi_\beta}{\partial t} \Delta t \right)}. \tag{28}$$

Solving Eq. (28) is straightforward because all variables on the right-hand side are known. In the noniterative model, the iterative application of the exchange term is unnecessary because the model suppresses deviations from the equal diffusion potential condition that stems from the conservation term. The governing equation for the phase-field variables remains consistent with that of the iterative model. The equations and characteristics of FID and iterative and noniterative models are concisely summarized in Fig. 1, including a flowchart detailing the numerical calculations. A comprehensive explanation of the flowchart is provided in Sec. III.

D. Diffusion equation and antitrapping current

Although iterative and noniterative models were derived from the FID model, the target of these models is a phenomenon where the equal diffusion potential condition is applicable. Therefore, we can use the governing equation of the composition field $\partial c^i / \partial t$ in the standard thin interface limit [28] model with an antitrapping current [25] as follows:

$$\frac{\partial c^i}{\partial t} = \nabla \cdot \sum_{\alpha=1}^N \phi_\alpha \sum_{j=1}^{n-1} D_\alpha^{ij} \nabla c_\alpha^j + \nabla \cdot \sum_{\alpha > \beta}^N \sum_{\beta=1}^N J_{\alpha\beta}^i, \tag{29}$$

where D_α^{ij} is the interdiffusion coefficient of components i and j in phase α, and $J_{\alpha\beta}^i$ is the antitrapping current of component i, which acts against the solute-trapping current between phases α and β. The multicomponent antitrapping current derived by Kim [29] was extended to our multiphase case:

$$J_{\alpha\beta}^i = \sum_{\beta=1}^N \frac{a_{\alpha\beta}}{\sqrt{2W_{\alpha\beta}}} \left(c_\alpha^i - c_\beta^i \right) \sqrt{\phi_\alpha \phi_\beta} \frac{\partial \phi_\alpha}{\partial t} \frac{\nabla(\phi_\alpha - \phi_\beta)}{|\nabla(\phi_\alpha - \phi_\beta)|}. \tag{30}$$

This equation is derived assuming no diffusion in phase β. The relationship between the phase-field and interface mobilities is derived under the thin-interface limit condition with the antitrapping current described by Eq. (30) as follows:

$$\frac{1}{m_{\alpha\beta}} = \frac{\sigma_{\alpha\beta}}{M_{\alpha\beta} a_{\alpha\beta}^2} - \frac{\pi}{8} \frac{a_{\alpha\beta}}{\sqrt{2W_{\alpha\beta}}} \zeta_{\alpha\beta}, \tag{31}$$

$$\zeta_{\alpha\beta} = \sum_{i=1}^{n-1} \left(c_\alpha^i - c_\beta^i \right) \sum_{j=1}^{n-1} \frac{\partial^2 f_\alpha}{\partial c_\alpha^i \partial c_\alpha^j} \sum_{k=1}^{n-1} d_\alpha^{jk} \left(c_\alpha^k - c_\beta^k \right), \tag{32}$$

where $m_{\alpha\beta}$ is the interface mobility and d_α^{jk} is the element of the inverse matrix of the interdiffusion matrix. In diffusion-controlled calculations ($m_{\alpha\beta} \to \infty$), the phase-field mobility becomes a function of the phase composition:

$$M_{\alpha\beta} = \frac{\pi^2}{\delta_{\alpha\beta}^2 \sum_{i=1}^{n-1} \left(c_\alpha^i - c_\beta^i \right) \sum_{j=1}^{n-1} \frac{\partial^2 f_\alpha}{\partial c_\alpha^i \partial c_\alpha^j} \sum_{k=1}^{n-1} d_\alpha^{jk} \left(c_\alpha^k - c_\beta^k \right)}, \tag{33}$$

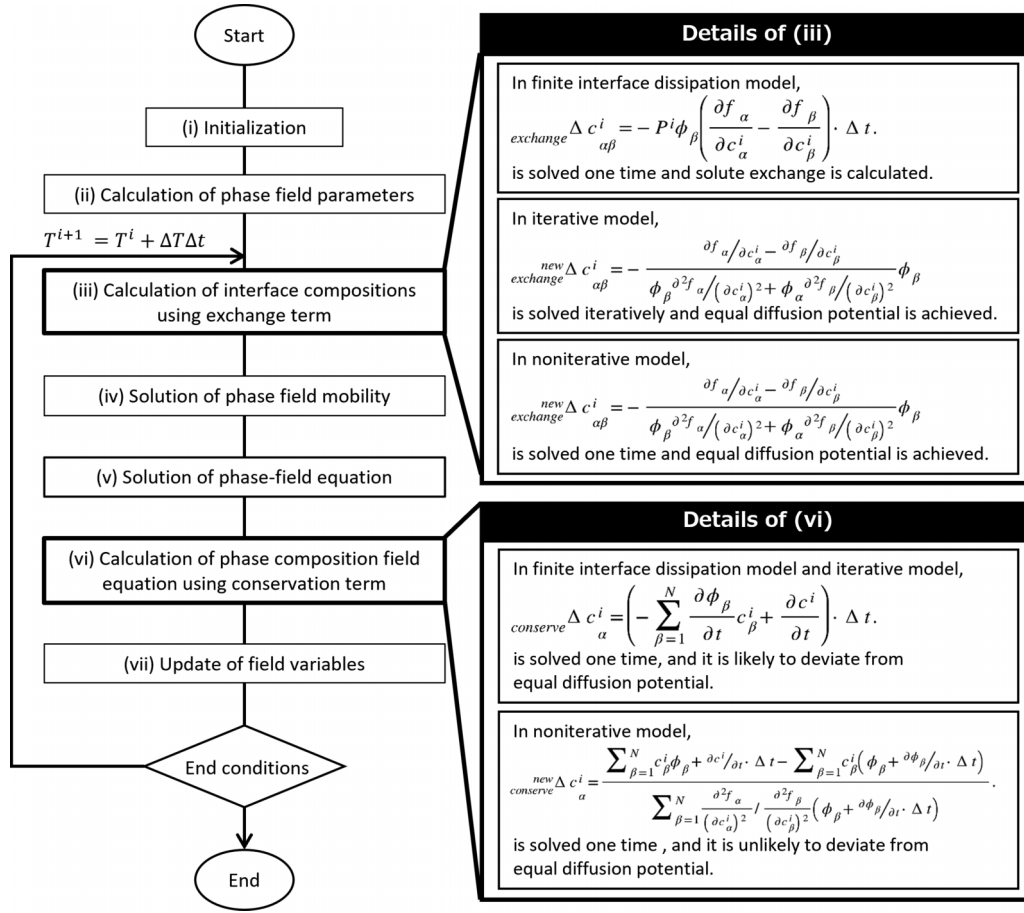at which the local equilibrium condition is maintained at the interface.

FIG. 1. Equations and characteristics of the three models described in Secs. II A, II B, and II C, along with a flowchart of the numerical calculations.

III. APPLICATION EXAMPLES

Several solidification problems were addressed to evaluate the validity and effectiveness of the two proposed models. The procedural steps, as outlined in the flowchart depicted in Fig. 1, were followed for the calculations. The process began with (i) setting the initial conditions for temperature, composition, and phase fields. Subsequently, (ii) the phase-field parameters were determined. Following this, (iii) phase compositions were derived by addressing the exchange term. Next, (iv) the phase-field mobility was ascertained using Eq. (31). This was followed by (v) calculating the temporal evolution of the phase field through the resolution of the phase-field equation. In step (vi), the time evolution of the phase composition field was computed by tackling the conservation term. Step (vii) involved updating the field variables, and (viii) repeat steps (iii)–(vii) were iteratively repeated. The governing equations were numerically solved employing a finite-difference scheme. For the iterative model, the calculations persisted until the norm of the exchange terms fell below 10^{-10} mol %.

For example, numerical tests were conducted on the Ag-Cu-Sn and Ni-Al-Cr systems. Moon [30] and Huang [31] developed the thermodynamic descriptions of each system, and the material parameters are listed in Tables I and II. In the Ni-Al-Cr system, the anisotropic energy of the fcc/liquid

interface is given as follows [32]:

$$\sigma(\theta) = \sigma(1 - 3\xi)$$
$$\times \left[1 + \frac{4\xi}{1 - 3\xi} \frac{(\partial\phi/\partial x)^4 + (\partial\phi/\partial y)^4 + (\partial\phi/\partial z)^4}{|\nabla\phi|^4} \right],$$
(34)

where ξ is the strength of the anisotropy.

The simulation code was developed using the Taichi programming language, a domain-specific language integrated within Python [33], to enhance computational efficiency significantly. Additionally, the computations were accelerated using an NVIDIA RTX A6000 GPU [34].

TABLE I. Material parameters for Ag-Cu-Sn system.

Quality	Symbol	Value
Initial composition of Cu	c_{Cu}	40.0 mol %
Initial composition of Sn	c_{Sn}	3.0 mol %
Diffusivity in liquid	D_L	$1.0 \times 10^{-9}\,\mathrm{m^2\,s^{-1}}$
Diffusivity in fcc	D_S	$1.0 \times 10^{-13}\,\mathrm{m^2\,s^{-1}}$
Interface energy	σ	$1.0\,\mathrm{J\,m^{-2}}$
Molar volume	V_m	$1.0 \times 10^{-5}\,\mathrm{m^3\,mol^{-1}}$

TABLE II. Material parameters for Ni-Al-Cr system.

Quality	Symbol	Value
Initial composition of Al	c_{Al}	20.0 mol %
Initial composition of Cr	c_{Cr}	5.0 mol %
Diffusivity in liquid	D_L	$1.0 \times 10^{-9} \, \mathrm{m^2 \, s^{-1}}$
Diffusivity in fcc	D_S	$1.0 \times 10^{-13} \, \mathrm{m^2 \, s^{-1}}$
Interface energy	σ	$1.0 \, \mathrm{J \, m^{-2}}$
Molar volume	V_m	$1.0 \times 10^{-5} \, \mathrm{m^3 \, mol^{-1}}$
Strength of anisotropy	ξ	0.03

A. Gibbs-Thomson effect in iterative and noniterative models

Initially, utilizing both iterative and noniterative models, we assessed the curvature effects on the solid-liquid equilibrium state in the Ni-Al-Cr system. A seed crystal was positioned at the corner of the computational domain, and the simulations were iterated until an equilibrium state was reached. For simplicity, interfacial anisotropy was not taken into account to obtain a constant radius of curvature. Variations in curvature were introduced by adjusting the grid resolution. Detailed information about the simulation setup can be found in Table III.

Curvature undercooling was ascertained by identifying the temperature at which the fcc phase composition aligned with the equilibrium composition without curvature effects. This value was then juxtaposed with the curvature undercooling predictions made by Gibbs-Thomson theory:

$$\Delta T_r = K\Gamma, \tag{35}$$

$$\Gamma = \frac{\sigma}{\Delta s_f} = \frac{\sigma T_f}{\Delta H_f}. \tag{36}$$

Here, K is the interface curvature, Γ is the Gibbs-Thomson coefficient, σ is the interface energy, and Δs_f and ΔH_f are entropy and enthalpy changes at transformation temperature T_f. The Gibbs-Thomson coefficient calculated by Eq. (36) is $1.83 \times 10^{-7} \, \mathrm{m \, K}$.

TABLE III. Calculation conditions in the test of Gibbs-Thomson effect.

Quality	Symbol	Value
Interface mobility	m	$\infty \, \mathrm{s \, mol \, J^{-1}}$
Initial temperature	T_{ini}	1644.62 K
Cooling rate	R	$0.0 \, \mathrm{K \, s^{-1}}$
Grid resolution	Δx	
a. Small curvature		$6.7 \times 10^{-9} \, \mathrm{m}$
b. Middle curvature		$1.0 \times 10^{-8} \, \mathrm{m}$
c. Large curvature		$2.0 \times 10^{-8} \, \mathrm{m}$
Interface thickness	η	$4.0 \times \Delta x \, \mathrm{m}$
Number of grids	$Nx = Ny$	64
Discrete time width	Δt	
a. Small curvature		$8.9 \times 10^{-9} \, \mathrm{s}$
b. Middle curvature		$2.0 \times 10^{-8} \, \mathrm{s}$
c. Large curvature		$8.0 \times 10^{-8} \, \mathrm{s}$

TABLE IV. Calculation conditions of 1D simulation in Ag-Cu-Sn system.

Quality	Symbol	Value
Interface mobility	m	$5.0 \times 10^{-11} \, \mathrm{s \, mol \, J^{-1}}$
Initial temperature	T_{ini}	1036.55 K
Cooling rate	R	$10.0 \, \mathrm{K \, s^{-1}}$
Grid resolution	Δx	$2.0 \times 10^{-7} \, \mathrm{m}$
Interface thickness	η	$8.0 \times 10^{-7} \, \mathrm{m}$
Number of grids	Nx	256
Discrete time width	Δt	$1.3 \times 10^{-5} \, \mathrm{s}$

B. Steady state in iterative, noniterative, and FID models

To assess the performance of the iterative and noniterative models against the conventional FID model in a steady state, 1D computational solidification experiments were conducted on a ternary Ag-Cu-Sn system. The objective was to ascertain whether the iterative and noniterative models could replicate the results of the conventional FID model when a sufficiently large interface permeability is assumed.

The simulation domain was set to a size of 51.2 μm with a grid resolution of 0.2 μm. Solidification commenced 1 K below the liquidus temperature at a constant cooling rate of 10 K s^{-1}. An Ag-rich fcc seed with a radius of 1 μm was placed at one end of the domain. The simulations were run with a time step of 1.0×10^5 applied, corresponding to a solidification duration of 1.3 s. Additional details regarding the simulation setup are provided in Table IV.

For the calculation of the FID model, Eqs. (17) and (39) from Ref. [22] were utilized owing to the complexity involved in solving Eqs. (6b) and (10b). Notably, the evolution of the phase-field variable and phase composition are interdependent processes. All one-dimensional (1D) solidification calculations for the Ag-Cu-Sn system were conducted without incorporating an antitrapping current.

C. Application to the simulation of microstructure evolution

The computational accuracy and efficiency of the noniterative model were benchmarked against an iterative model, which incorporates convergence calculations to satisfy the equal diffusion potential condition. These models have been employed to simulate two microstructure formation processes in practical alloys.

One application involved a 2D eutectic growth simulation within a multiphase Ag-Cu-Sn system. The simulation domain measured 25.6 μm × 25.6 μm with a grid resolution of 0.2 μm. Solidification was initiated 1 K below the liquidus temperature at a constant cooling rate of 5 K s^{-1}. Ag-rich and Cu-rich fcc seeds, each with a radius of 1 μm, were arranged with a spacing of 3.2 μm. A time step of 2.0×10^5 was utilized, equating to a solidification duration of 1.6 s. Additional specifics of the Ag-Cu-Sn system simulation setup are detailed in Table V.

Another application area includes 2D and 3D dendrite growth simulations for the Ni-Al-Cr system. In the 2D scenario, the simulation domain was 25.6 μm × 25.6 μm, with a grid resolution of 0.1 μm. Solidification started 5 K below

TABLE V. Calculation conditions of 2D simulation in Ag-Cu-Sn system.

Quality	Symbol	Value
Interface mobility between liquid and fcc	m	∞ s mol J^{-1}
Phase-field mobility between fcc and fcc	M	1.0×10^{-5} m^3 J^{-1} s^{-1}
Initial temperature	T_{ini}	1036.55 K
Cooling rate	R	5.0 K s^{-1}
Grid resolution	Δx	2.0×10^{-7} m
Interface thickness	η	8.0×10^{-7} m
Number of grids	$Nx = Ny$	128
Discrete time width	Δt	8.0×10^{-6} s

the liquidus temperature at a cooling rate of 50 K/s. A fcc seed with a radius of 0.5 μm was positioned at one corner of the domain. Simulations were conducted with a time step of 4.0×10^4, corresponding to a solidification time of 8.0×10^{-2} s. Further information on the 2D dendrite growth simulation setup for the Ni-Al-Cr system is available in Table VI.

In the 3D simulation, the domain measured 51.2 μm × 51.2 μm × 102.4 μm, with a grid resolution of 0.2 μm. Solidification was initiated 5 K below the liquidus temperature, maintaining a constant cooling rate of 50 K s^{-1}. At the outset, a fcc seed with a radius of 0.5 μm was positioned at the bottom center of the domain. A time step of 3.0×10^4 was applied, corresponding to a solidification time of 1.7×10^{-1} s. Stochastic noise was introduced to the driving force governing the phase-field evolution to facilitate the formation of secondary arms. Additional specifics of the simulation setup are provided in Table VII.

The practicality of the noniterative model was assessed based on numerical computation speed and the magnitude of errors observed. These errors were quantified as the discrepancy in the fcc fraction and, specifically in the 2D simulation, the difference in the composition profile between the iterative and noniterative models.

IV. RESULTS AND DISCUSSION

A. Gibbs-Thomson effect in iterative and noniterative models

The equilibrium shape of the fcc phase becomes spherical, with its composition varying in response to curvature.

TABLE VI. Calculation conditions of 2D simulation in Ni-Al-Cr system.

Quality	Symbol	Value
Interface mobility	m	∞ s mol J^{-1}
Initial temperature	T_{ini}	1644.62 K
Cooling rate	R	50.0 K s^{-1}
Grid resolution	Δx	1.0×10^{-7} m
Interface thickness	η	4.0×10^{-7} m
Number of grids	$Nx = Ny$	256
Discrete time width	Δt	2.0×10^{-6} s

TABLE VII. Calculation conditions of 3D simulations in Ni-Al-Cr system.

Quality	Symbol	Value
Interface mobility	m	∞ s mol J^{-1}
Initial temperature	T_{ini}	1644.62 K
Cooling rate	R	50.0 K s^{-1}
Temperature gradient	G	1.0×10^5 K m^{-1}
Grid resolution	Δx	2.0×10^{-7} m
Interface thickness	η	8.0×10^{-7} m
Number of grids	$Nx = Ny$	256
Number of grids	Nz	512
Discrete time width	Δt	5.7×10^{-6} s

Such curvature undercooling was quantified for each component because, in multicomponent systems, curvature effects alter the equilibrium composition, causing it to diverge from the equilibrium composition at other temperatures. Figure 2 illustrates the outcomes derived from both iterative and noniterative models. The circular plots depict the curvature undercooling based on the Al composition in the fcc phase, while the triangular plots represent the undercooling calculated using the Cr composition in the fcc phase. For scenarios of zero curvature, a 1D calculation was executed, yielding a fraction, Al composition, and Cr composition in the fcc phase of 0.217, 18.2 mol %, and 4.55 mol %, respectively. These figures align with the equilibrium calculations conducted using pycalphad [35]. The line in the graph signifies the curvature undercooling as predicted by the Gibbs-Thomson theory [Eq. (35)]. The proximity of the plots to this line corroborates the capability of the developed models to replicate the Gibbs-Thomson effect accurately. As depicted in Fig. 3, the equilibrium shape exhibiting an anisotropy strength of 0.05 obtained using by iterative [Fig. 3(a)] and noniterative [Fig. 3(b)] models (solid black line) were aligned with that obtained using the analytical solution provided by Eq. (2) in [36] (dashed white line). These two lines overlap completely and appear as a single line.

B. Steady state in iterative, noniterative, and FID models

Figure 4 presents the temperature-dependent fraction of the fcc phase as determined by the iterative and noniterative models alongside the FID model. The outcomes from the FID model align with those of the iterative and noniterative models as the interface permeability increases. The maximum interface permeabilities necessary for stable computations were found to be $P^{Cu} = 3.0 \times 10^{-5}$ m^3 J^{-1} s^{-1} and $P^{Sn} = 2.0 \times 10^{-6}$ m^3 J^{-1} s^{-1}. With these interface permeability levels, the FID model produced results equivalent to the iterative and noniterative models. Consequently, it is demonstrated that both iterative and noniterative models can fulfill the equal diffusion potential condition without needing to adjust the interface permeability.

C. Application to the simulation of microstructure evolution

Figure 5 illustrates the composition distribution as determined by the iterative model and the composition profiles
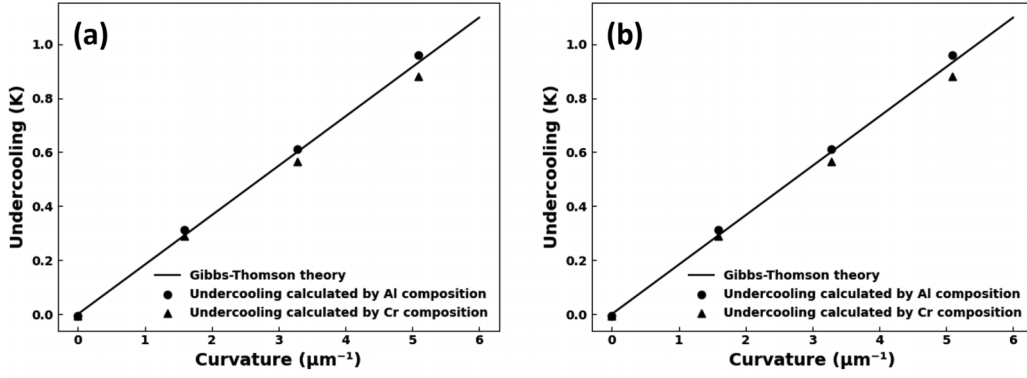
FIG. 2. Curvature undercooling of (a) iterative and (b) noniterative models calculated by Al and Cr compositions and Gibbs-Thomson theory in Ni-Al-Cr system.

generated using both the iterative and noniterative models. The horizontal axes for the latter are aligned with the direction indicated by the arrows in the former's composition distribution. Solid lines denote the composition profiles obtained from the iterative model, while dashed lines represent those calculated by the noniterative model. As depicted in Fig. 5, the noniterative model exhibits no variation in composition distribution, mirroring the uniform composition distribution observed in the iterative model. Figures 5(a) and 5(b) demonstrate that the position of the interface, the compositions within the fcc phase, and the morphology of the diffusion layer as determined by the noniterative model closely align with those derived from the iterative model. Furthermore, in Figs. 5(c) and 5(d), the fluctuations observed in the liquid phase composition near the eutectic interfaces are consistently represented in both models. In particular, as shown in Fig. 5(d), subtle fluctuations on the order of 10^{-5} mol % are consistent. Here, the errors in the fraction of the fcc phase are calculated as

$$f_{\text{Noniterative}} - f_{\text{Iterative}}, \tag{37}$$

where $f_{\text{Iterative}}$ and $f_{\text{Noniterative}}$ are the fractions of fcc calculated using the iterative and noniterative models, respectively. Throughout the simulation, the errors were not larger than 1.2×10^{-6} in the 2D calculation of the Ag-Cu-Sn system and 2.8×10^{-7} in the 2D calculation of the Ni-Al-Cr system. Although the noniterative model does not use convergence calculations, the results are consistent with the iterative model,

which uses convergence calculations to ensure equal diffusion potential conditions.

Figure 6 displays the morphologies of fcc dendrites in the 3D simulation of the Ni-Al-Cr system at solidification times of 2.8×10^{-2}, 8.6×10^{-2}, and 1.7×10^{-1} s, as predicted by the iterative model. The competitive growth observed among multiple dendrites originated from a single fcc seed. The growth of dendrite arms was inhibited when they were in close proximity, whereas secondary arms developed when the arms were more sparsely distributed. The 3D simulation quantified discrepancies between the iterative and noniterative models using Eq. (37). Throughout the simulation, the observed errors did not exceed 1.9×10^{-3}. The increased error compared to 2D simulations could be attributed to the synergistic effect of secondary arm growth and stochastic noise in the driving force for phase-field evolution, yet this error remained negligibly small.

Table VIII outlines the computational times for each simulation. The 3D simulations required relatively short durations of 159.1 min for the iterative model and 53.3 min for the noniterative model. Across all simulations, the noniterative model demonstrated superior speed to the iterative model.
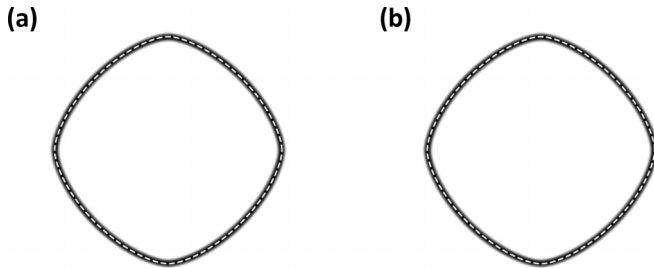

FIG. 3. Equilibrium shape with an anisotropy of 0.05 obtained by (a) iterative and (b) noniterative models (solid black line) and the analytical solution (dashed white line).
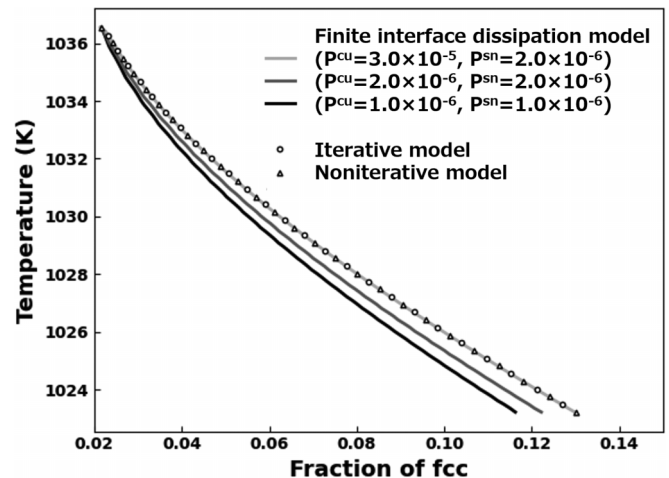

FIG. 4. Temperature dependence of the fraction of fcc phase in three models in 1D solidification of Ag-Cu-Sn system.
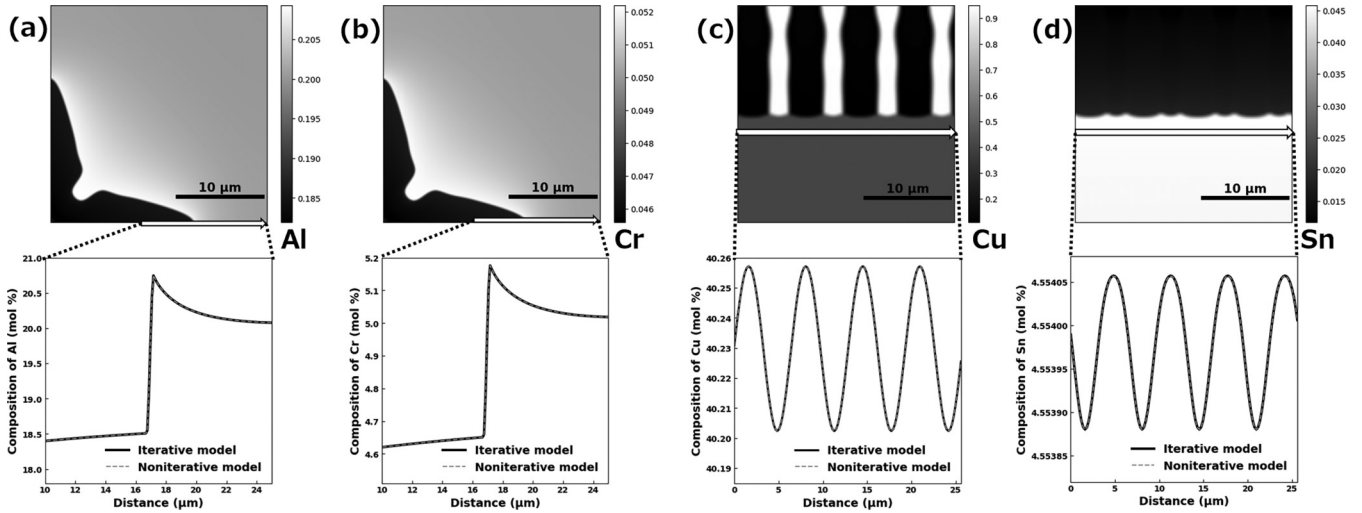
FIG. 5. Composition distribution and composition profile of (a) Al, (b) Cr, (c) Cu, and (d) Sn at a solidification time of 8.0×10^{-2} s in the calculation of dendrite growth in Ni-Al-Cr system and 1.6 s in the calculation of eutectic growth in Ag-Cu-Sn system. The composition distribution is the result of the iterative model, while the composition profile results from both iterative and noniterative models.

This efficiency stems from the noniterative model's avoidance of convergence calculations with conditional branches, enabling more efficient parallel computations by the GPU.

V. CONCLUSIONS

We introduced a different approach for directly coupling the CALPHAD database with phase-field modeling, deriving two models to ensure equal diffusion potential conditions by adapting the governing equations of the finite interface dissipation model. The iterative model utilizes convergence calculations to meet the equal diffusion potential condition, whereas the noniterative model eliminates the need for such calculations. Key characteristics of these models include (i) the elimination of preliminary calculations, (ii) the assurance of equal diffusion potential conditions, (iii) the ability to directly apply CALPHAD functions, and (iv) the absence of additional parameters, such as interface permeability in the FID model and recalculation intervals in the extrapolation method.
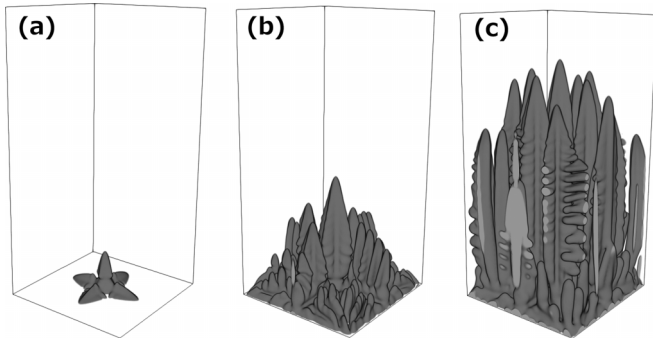

FIG. 6. Dendrite growth of a single fcc seed in Ni-Al-Cr system at solidification time of (a) 2.8×10^{-2} s, (b) 8.6×10^{-2} s, and (c) 1.7×10^{-1} s calculated by iterative model.

To validate the computational accuracy and efficiency of these models, case studies were performed focusing on the solidification processes in Ag-Cu-Sn and Ni-Al-Cr systems. The findings from these studies are summarized below.

(1) The iterative and noniterative models effectively replicated the Gibbs-Thomson effect.

(2) The results of the iterative and noniterative models were consistent with those of the FID model, with the highest interface permeabilities required for stable computation.

(3) The discrepancy in the fraction of the fcc phase between the iterative and noniterative models was negligible, indicating high accuracy in phase fraction predictions. Additionally, differences in the composition profiles between the models were not visually discernible, further attesting to their precision. Utilizing the NVIDIA RTX A6000 GPU, the 3D dendrite growth simulation, encompassing steps on a $256 \times 256 \times 512$ grid, was completed in 159.1 and 53.3 min by the iterative and noniterative models, respectively. This showcases the significant computational efficiency of the noniterative model, attributed to its streamlined calculation process that bypasses the need for convergence calculations.

The model proposed in this study is applicable for substitutional solution phases wherein the free energy is assessed as a function of solute concentration and temperature, however,

TABLE VIII. Computational time for each simulation.

	Iterative model	Noniterative model
2D dendrite growth in Ni-Al-Cr system	87 s	66 s
2D eutectic growth in Ag-Cu-Sn system	472 s	317 s
3D dendrite growth in Ni-Al-Cr system	159.1 min	53.3 min

is not implementable for intermetallic compounds and interstitial solute phases described by the CALPHAD sublattice approach. Future work will address the extension of the model to the CALPHAD sublattice approach.

APPENDIX A: DETAILED DERIVATION OF EQ. (15)

In this appendix, we show how Eq. (15) is obtained from Eq. (14b) in Sec. III. Equations (11) and (12) yield the following equations:

$$\frac{\partial c_\alpha^i}{\partial x^i} = \phi_\beta, \tag{A1}$$

$$\frac{\partial c_\beta^i}{\partial x^i} = -\phi_\alpha. \tag{A2}$$

Ignoring higher orders and applying the chain rule in Eq. (14b), we obtain

$$
\begin{aligned}
H^i(x^1, \ldots, x^{n-1}) &= \frac{\partial f_\alpha}{\partial c_\alpha^i}\left(c_\alpha^1\big|_t, \ldots, c_\alpha^{n-1}\big|_t\right) - \frac{\partial f_\beta}{\partial c_\beta^i}\left(c_\beta^1\big|_t, \ldots, c_\beta^{n-1}\big|_t\right) + \left(x^1\frac{\partial}{\partial x^1} + \cdots + x^{n-1}\frac{\partial}{\partial x^{n-1}}\right) \\
&\quad \times \left[\frac{\partial f_\alpha}{\partial c_\alpha^i}\left(c_\alpha^1\big|_t, \ldots, c_\alpha^{n-1}\big|_t\right) - \frac{\partial f_\beta}{\partial c_\beta^i}\left(c_\beta^1\big|_t, \ldots, c_\beta^{n-1}\big|_t\right)\right] \\
&= \frac{\partial f_\alpha}{\partial c_\alpha^i}\left(c_\alpha^1\big|_t, \ldots, c_\alpha^{n-1}\big|_t\right) - \frac{\partial f_\beta}{\partial c_\beta^i}\left(c_\beta^1\big|_t, \ldots, c_\beta^{n-1}\big|_t\right) \\
&\quad + \left(x^1\frac{\partial}{\partial c_\alpha^1}\frac{\partial c_\alpha^1}{\partial x^1} + \cdots + x^{n-1}\frac{\partial}{\partial c_\alpha^{n-1}}\frac{\partial c_\alpha^{n-1}}{\partial x^{n-1}}\right)\frac{\partial f_\alpha}{\partial c_\alpha^i}\left(c_\alpha^1\big|_t, \ldots, c_\alpha^{n-1}\big|_t\right) \\
&\quad - \left(x^1\frac{\partial}{\partial c_\beta^1}\frac{\partial c_\beta^1}{\partial x^1} + \cdots + x^{n-1}\frac{\partial}{\partial c_\beta^{n-1}}\frac{\partial c_\beta^{n-1}}{\partial x^{n-1}}\right)\frac{\partial f_\beta}{\partial c_\beta^i}\left(c_\beta^1\big|_t, \ldots, c_\beta^{n-1}\big|_t\right).
\end{aligned}
\tag{A3, A4}
$$

By substituting Eqs. (A1) and (A2) into Eq. (A4), the following equation is obtained:

$$
\begin{aligned}
H^i(x^1, \ldots, x^{n-1}) &= \frac{\partial f_\alpha}{\partial c_\alpha^i}\left(c_\alpha^1\big|_t, \ldots, c_\alpha^{n-1}\big|_t\right) - \frac{\partial f_\beta}{\partial c_\beta^i}\left(c_\beta^1\big|_t, \ldots, c_\beta^{n-1}\big|_t\right) + \phi_\beta\left(x^1\frac{\partial}{\partial c_\alpha^1} + \cdots + x^{n-1}\frac{\partial}{\partial c_\alpha^{n-1}}\right)\frac{\partial f_\alpha}{\partial c_\alpha^i}\left(c_\alpha^1\big|_t, \ldots, c_\alpha^{n-1}\big|_t\right) \\
&\quad + \phi_\alpha\left(x^1\frac{\partial}{\partial c_\beta^1} + \cdots + x^{n-1}\frac{\partial}{\partial c_\beta^{n-1}}\right)\frac{\partial f_\beta}{\partial c_\beta^i}\left(c_\beta^1\big|_t, \ldots, c_\beta^{n-1}\big|_t\right).
\end{aligned}
\tag{A5}
$$

APPENDIX B: ANALYTICAL SOLUTION OF x^i WITHOUT NEGLECTING CROSS TERMS

Although we ignored cross terms to derive the exchange term in this study, the analytical solution of the exchange term can also be obtained without this simplification. Using Eq. (A5), the equal diffusion potential condition for each component can be expressed as follows:

$$
H^1(x^1, \ldots, x^{n-1}) = \frac{\partial f_\alpha}{\partial c_\alpha^1} - \frac{\partial f_\beta}{\partial c_\beta^1} + \phi_\beta\left(x^1\frac{\partial}{\partial c_\alpha^1} + \cdots + x^{n-1}\frac{\partial}{\partial c_\alpha^{n-1}}\right)\frac{\partial f_\alpha}{\partial c_\alpha^1} + \phi_\alpha\left(x^1\frac{\partial}{\partial c_\beta^1} + \cdots + x^{n-1}\frac{\partial}{\partial c_\beta^{n-1}}\right)\frac{\partial f_\beta}{\partial c_\beta^1} = 0,
$$

$$\vdots$$

$$
\begin{aligned}
H^{n-1}(x^1, \ldots, x^{n-1}) &= \frac{\partial f_\alpha}{\partial c_\alpha^{n-1}} - \frac{\partial f_\beta}{\partial c_\beta^{n-1}} + \phi_\beta\left(x^1\frac{\partial}{\partial c_\alpha^1} + \cdots + x^{n-1}\frac{\partial}{\partial c_\alpha^{n-1}}\right)\frac{\partial f_\alpha}{\partial c_\alpha^{n-1}} + \phi_\alpha\left(x^1\frac{\partial}{\partial c_\beta^1} + \cdots + x^{n-1}\frac{\partial}{\partial c_\beta^{n-1}}\right)\frac{\partial f_\beta}{\partial c_\beta^{n-1}} \\
&= 0.
\end{aligned}
\tag{B1}
$$

Equation (B1) can be solved with respect to x^i as follows:

$$\therefore \begin{pmatrix} x^1 \\ \vdots \\ x^{n-1} \end{pmatrix} = -\begin{pmatrix} \phi_\beta \frac{\partial^2 f_\alpha}{\partial c_\alpha^1 c_\alpha^1} + \phi_\alpha \frac{\partial^2 f_\beta}{\partial c_\beta^1 c_\beta^1} & \cdots & \phi_\beta \frac{\partial^2 f_\alpha}{\partial c_\alpha^{n-1} c_\alpha^1} + \phi_\alpha \frac{\partial^2 f_\beta}{\partial c_\beta^{n-1} c_\beta^1} \\ \vdots & \ddots & \vdots \\ \phi_\beta \frac{\partial^2 f_\alpha}{\partial c_\alpha^1 c_\alpha^{n-1}} + \phi_\alpha \frac{\partial^2 f_\beta}{\partial c_\beta^1 c_\beta^{n-1}} & \cdots & \phi_\beta \frac{\partial^2 f_\alpha}{\partial c_\alpha^{n-1} c_\alpha^{n-1}} + \phi_\alpha \frac{\partial^2 f_\beta}{\partial c_\beta^{n-1} c_\beta^{n-1}} \end{pmatrix}^{-1} \begin{pmatrix} \frac{\partial f_\alpha}{\partial c_\alpha^1} - \frac{\partial f_\beta}{\partial c_\beta^1} \\ \vdots \\ \frac{\partial f_\alpha}{\partial c_\alpha^{n-1}} - \frac{\partial f_\beta}{\partial c_\beta^{n-1}} \end{pmatrix}. \tag{B2}$$

[1] R. Kobayashi, Modeling and numerical simulations of dendritic crystal growth, Phys. D (Amsterdam, Neth.) **63**, 410 (1993).

[2] A. A. Wheeler, W. J. Boettinger, and G. B. McFadden, Phase-field model for isothermal phase transitions in binary alloys, Phys. Rev. A **45**, 7424 (1992).

[3] A. A. Wheeler, G. B. McFadden, and W. J. Boettinger, Phase-field model for solidification of a eutectic alloy, Proc. R. Soc. London, Ser. A **452**, 495 (1996).

[4] S. G. Kim, W. T. Kim, and T. Suzuki, Phase-field model for binary alloys, Phys. Rev. E **60**, 7186 (1999).

[5] M. Ode, J. S. Lee, S. G. Kim, W. T. Kim, and T. Suzuki, Phase-field model for solidification of ternary alloys, ISIJ Int. **40**, 870 (2000).

[6] J. Tiaden, B. Nestler, H. J. Diepers, and I. Steinbach, The multiphase-field model with an integrated concept for modelling solute diffusion, Phys. D (Amsterdam, Neth.) **115**, 73 (1998).

[7] I. Steinbach and F. Pezzolla, A generalized field method for multiphase transformations using interface fields, Phys. D (Amsterdam, Neth.) **134**, 385 (1999).

[8] I. Steinbach, F. Pezzolla, B. Nestler, M. Seeßelberg, R. Prieler, G. J. Schmitz, and J. L. L. Rezende, A phase field concept for multiphase systems, Phys. D (Amsterdam, Neth.) **94**, 135 (1996).

[9] U. Grafe, B. Böttger, J. Tiaden, and S. G. Fries, Coupling of multicomponent thermodynamic databases to a phase field model: application to solidification and solid state transformations of superalloys, Scr. Mater. **42**, 1179 (2000).

[10] I. Steinbach, B. Böttger, J. Eiken, N. Warnken, and S. G. Fries, CALPHAD and phase-field modeling: A successful liaison, J. Phase Equilib. Diffus. **28**, 101 (2007).

[11] H. Kobayashi, M. Ode, S. Gyoon Kim, W. Tae Kim, and T. Suzuki, Phase-field model for solidification of ternary alloys coupled with thermodynamic database, Scr. Mater. **48**, 689 (2003).

[12] S. Nomoto, M. Kusano, H. Kitano, and M. Watanabe, Multi-phase field method for solidification microstructure evolution for a Ni-based alloy in wire arc additive manufacturing, Metals **12**, 1720 (2022).

[13] M. Uddagiri, O. Shchyglo, I. Steinbach, and M. Tegeler, Solidification of the Ni-based superalloy CMSX-4 simulated with full complexity in 3-dimensions, Prog. Addit. Manuf. (2023), doi:10.1007/s40964-023-00513-9.

[14] J. Eiken, B. Böttger, and I. Steinbach, Multiphase-field approach for multicomponent alloys with extrapolation scheme for numerical application, Phys. Rev. E **73**, 066122 (2006).

[15] B. Böttger, J. Eiken, and M. Apel, Multi-ternary extrapolation scheme for efficient coupling of thermodynamic data to a multi-phase-field model, Comput. Mater. Sci. **108**, 283 (2015).

[16] C. Yang, Q. Xu, and B. Liu, A high precision extrapolation method in multiphase-field model for simulating dendrite growth, J. Cryst. Growth **490**, 25 (2018).

[17] C. Yang, X. Wang, J. Wang, and H. Huang, Multiphase-field approach with parabolic approximation scheme, Comput. Mater. Sci. **172**, 109322 (2020).

[18] C. Yang, J. Wang, H. Xing, and H. Huang, A parabolic approximation scheme for multi-phase-filed simulation of non-isothermal solidification, Mater. Today Commun. **28**, 102712 (2021).

[19] X. Jiang, R. Zhang, C. Zhang, H. Yin, and X. Qu, Fast prediction of the quasi phase equilibrium in phase field model for multicomponent alloys based on machine learning method, Calphad **66**, 101644, (2019).

[20] L. Ren, S. Geng, P. Jiang, S. Gao, and C. Han, Numerical simulation of dendritic growth during solidification process using multiphase-field model aided with machine learning method, Calphad **78**, 102450 (2022).

[21] I. Steinbach, L. Zhang, and M. Plapp, Phase-field model with finite interface dissipation, Acta Mater. **60**, 2689 (2012).

[22] L. Zhang and I. Steinbach, Phase-field model with finite interface dissipation: Extension to multi-component multi-phase alloys, Acta Mater. **60**, 2702 (2012).

[23] M. Segawa, A. Yamanaka, and S. Nomoto, Multi-phase-field simulation of cyclic phase transformation in Fe-C-Mn and Fe-C-Mn-Si alloys, Comput. Mater. Sci. **136**, 67 (2017).

[24] S. Nomoto, M. Segawa, and M. Watanabe, Non- and quasi-equilibrium multi-phase field methods coupled with CALPHAD database for rapid-solidification microstructural evolution in laser powder bed additive manufacturing condition, Metals **11**, 626 (2021).

[25] A. Karma, Phase-field formulation for quantitative modeling of alloy solidification, Phys. Rev. Lett. **87**, 115701 (2001).

[26] B. Echebarria, R. Folch, A. Karma, and M. Plapp, Quantitative phase-field model of alloy solidification, Phys. Rev. E **70**, 061604 (2004).

[27] T. Koyama, Y. Tsukada, T. Abe, and Y. Kobayashi, Phase-field simulation on the formation of grain boundary phase in neodymium hard magnet, J. Jpn. Inst. Met. **81**, 43 (2017) [in Japanese].

[28] A. Karma and W.-J. Rappel, Quantitative phase-field modeling of dendritic growth in two and three dimensions, Phys. Rev. E **57**, 4323 (1998).

[29] S. G. Kim, A phase-field model with antitrapping current for multicomponent alloys with arbitrary thermodynamic properties, Acta Mater. **55**, 4391 (2007).

[30] K.-W. Moon, W. J. Boettinger, U. R. Kattner, F. S. Biancaniello, and C. A. Handwerker, Experimental and thermodynamic assessment of Sn-Ag-Cu solder alloys, J. Electron. Mater. **29**, 1122 (2000).

[31] W. Huang and Y. A. Chang, Thermodynamic properties of the Ni–Al–Cr system, Intermetallics **7**, 863 (1999).

[32] T. Takaki, S. Sakane, M. Ohno, Y. Shibuta, T. Shimokawabe, and T. Aoki, Primary arm array during directional solidification of a single-crystal binary alloy: Large-scale phase-field study, Acta Mater. **118**, 230 (2016).

[33] Y. Hu, T.-M. Li, L. Anderson, J. Ragan-Kelley, and F. Durand, Taichi: A language for high-performance computation on spatially sparse data structures, ACM Trans. Graph. **38**, 1 (2019).

[34] A. Yamanaka, T. Aoki, S. Ogawa, and T. Takaki, GPU-accelerated phase-field simulation of dendritic solidification in a binary alloy, J. Cryst. Growth **318**, 40 (2011).

[35] R. Otis and Z.-K. Liu, Pycalphad: CALPHAD-based computational thermodynamics in python, J. Open Res. Softw. **5**, 1 (2017).

[36] J. J. Eggleston, G. B. McFadden, and P. W. Voorhees, A phase-field model for highly anisotropic interfacial energy, Phys. D (Amsterdam, Neth.) **150**, 91 (2001).

[37] www.editage.jp.